minerals

MDPI

Article

Mineralogical Study of the Advanced Argillic Alteration Zone at the Konos Hill Mo–Cu–Re–Au Porphyry Prospect, NE Greece †

Constantinos Mavrogonatos [1,*], Panagiotis Voudouris [1], Paul G. Spry [2], Vasilios Melfos [3], Stephan Klemme [4], Jasper Berndt [4], Tim Baker [5], Robert Moritz [6], Thomas Bissig [7], Thomas Monecke [8] and Federica Zaccarini [9]

1 Faculty of Geology & Geoenvironment, National and Kapodistrian University of Athens, 15784 Athens, Greece; voudouris@geol.uoa.gr
2 Department of Geological and Atmospheric Sciences, Iowa State University, Ames, IA 50011, USA; pgspry@iastate.edu
3 Faculty of Geology, Aristotle University of Thessaloniki, 54124 Thessaloniki, Greece; melfosv@geo.auth.gr
4 Institut für Mineralogie, Westfälische Wilhelms-Universität Münster, 48149 Münster, Germany; Stephan.Klemme@uni-muenster.de (S.K.); jberndt@uni-muenster.de (J.B.)
5 Eldorado Gold Corporation, 1188 Bentall 5 Burrard St., Vancouver, BC V6C 2B5, Canada; timb@eldoradogold.com
6 Department of Mineralogy, University of Geneva, CH-1205 Geneva, Switzerland; Robert.Moritz@unige.ch
7 Goldcorp Inc., Park Place, Suite 3400-666, Burrard St., Vancouver, BC V6C 2X8, Canada; ThomasBissig@goldcorp.com
8 Center for Mineral Resources Science, Department of Geology and Geological Engineering, Colorado School of Mines, 1516 Illinois Street, Golden, CO 80401, USA; tmonecke@mines.edu
9 Department of Applied Geosciences and Geophysics, University of Leoben, Leoben 8700, Austria; federica.zaccarini@unileoben.ac.at
* Correspondence: kmavrogon@geol.uoa.gr; Tel.: +30-698-860-8161
† The paper is an extended version of our paper published in 1st International Electronic Conference on Mineral Science, 16–21 July 2018.

Received: 8 October 2018; Accepted: 22 October 2018; Published: 24 October 2018

Abstract: The Konos Hill prospect in NE Greece represents a telescoped Mo–Cu–Re–Au porphyry occurrence overprinted by deep-level high-sulfidation mineralization. Porphyry-style mineralization is exposed in the deeper parts of the system and comprises quartz stockwork veins hosted in subvolcanic intrusions of granodioritic composition. Ore minerals include pyrite, molybdenite, chalcopyrite, and rheniite. In the upper part of the system, intense hydrothermal alteration resulted in the formation of a silicified zone and the development of various advanced argillic alteration assemblages, which are spatially related to N–S, NNW–SSE, and E–W trending faults. More distal and downwards, advanced argillic alteration gradually evolves into phyllic assemblages dominated by quartz and sericite. Zunyite, along with various amounts of quartz, alunite, aluminum phosphate–sulfate minerals (APS), diaspore, kaolinite, and minor pyrophyllite, are the main minerals in the advanced argillic alteration. Mineral-chemical analyses reveal significant variance in the SiO_2, F, and Cl content of zunyite. Alunite supergroup minerals display a wide compositional range corresponding to members of the alunite, beudantite, and plumbogummite subgroups. Diaspore displays an almost stoichiometric composition. Mineralization in the lithocap consists of pyrite, enargite, tetrahedrite/tennantite, and colusite. Bulk ore analyses of mineralized samples show a relative enrichment in elements such as Se, Mo, and Bi, which supports a genetic link between the studied lithocap and the underlying Konos Hill porphyry-style mineralization. The occurrence of advanced argillic alteration assemblages along the N–S, NNW–SSE, and E–W trending faults suggests that highly acidic hydrothermal fluids were ascending into the lithocap environment. Zunyite, along with diaspore, pyrophyllite, and Sr- and

Rare Earth Elements-bearing APS minerals, mark the proximity of the hypogene advanced argillic alteration zone to the porphyry environment.

Keywords: zunyite; alunite supergroup minerals; lithocap; porphyry-epithermal mineralization; Greece

1. Introduction

Porphyry deposits are characterized by a zonation of mineralization and associated types of hydrothermal alteration. In most deposits, this zonation comprises an inner, strongly mineralized part hosted by potassic alteration, which is outwardly replaced by sericitic and more distally by propylitic assemblages, the latter being commonly dominated by epidote and chlorite [1]. This spatial succession of alteration types reflects the cooling of the hydrothermal fluids and, to some extent, their possible mixing with meteoric fluids [2,3].

In many cases, advanced argillic alteration zones, or "lithocaps" [4], develop at shallow levels above porphyry Cu–Au deposits (e.g., Lepanto-Far Southeast, Philippines [5]; Maricunga, Chile [6]). Advanced argillic alteration mineral assemblages precipitate from SO_2- and HCl-rich magmatic vapor, which arises from an underlying intrusive source. The vapor condenses into near-surface fluids in a relatively shallow environment [7,8], where leaching of the host rock by the most acidic condensate leaves residual silica that recrystallizes to quartz and forms the core of the alteration [8]. In cases where such fluids affect porphyritic magmatic rocks, commonly, the result is vuggy textures.

These lithocaps are favorable environments for exploration, as they can host high-sulfidation ores and can be located spatially adjacent to porphyry-style mineralization [9,10]. Commonly, they comprise various amounts of quartz, andalusite, pyrophyllite, topaz, kaolinite–dickite, diaspore, corundum, zunyite, tourmaline, alunite supergroup minerals, and dumortierite [11–13]. Lithocaps are usually zoned. In the deep parts, quartz and pyrophyllite occur, commonly transitioning downwards to porphyry-related sericitic alteration [14], which hosts pyrite veinlets with silica–sericite selvedges (described also as "D-type" veins) [6,9]. In shallow levels, quartz and alunite predominate [13].

Advanced argillic alteration zones commonly overlie or overprint earlier alteration styles in many porphyry systems [15]. This telescoping has been attributed to rapid collapse of the isotherms, due to the retreat of the magma interface [16] or to the waning convection from the magmatic body at depth [17], with exogenic factors such as rapid uplift and erosion or collapse of the volcanic edifice also playing important roles [18]. Advanced argillic alteration lithocaps have been described from a number of porphyry-epithermal deposits and prospects worldwide, and coupled with the occurrence of a transitional to sericitic alteration zone, they mark the change from the high-sulfidation epithermal to the porphyry environment. Examples include the Hugo Dummett deposit in Mongolia [15], El Salvador in Chile [10], and Rosia Poieni in Romania [19].

In Greece, several advanced argillic alteration lithocaps have been identified [20,21]. The best-known example is in the Kassiteres-Sapes district [22–24], where advanced argillic alteration zones host significant, high-to-intermediate-sulfidation ores (e.g., the Viper Au–Cu–Ag–Te deposit [25]), which overprint or form laterally to porphyry-style mineralization [23,26,27]. Other examples include the Mavrokoryfi [28] and Melitena [29] prospects in the Thrace district, northeastern Greece, as well as the Fakos and Stypsi prospects on Limnos and Lesvos islands, respectively [30–32].

Zunyite is a relatively rare mineral in advanced argillic alteration assemblages. It is a F- and Cl-bearing aluminosilicate [$Al_{13}Si_5O_{20}(OH,F)_{18}Cl$] that was originally described from and named after the Zuni mine at Anvil Mountain, CO, USA [33]. The presence of zunyite in Greece was documented previously from Kos Island [34], where it occurs in advanced argillic-altered rhyolites and at the Konos Hill porphyry Mo–Cu–Re–Au system [35]. The latter is the only known occurrence of zunyite in a lithocap that occurs above a porphyry system in Greece.

This study is an extended version of a paper by Mavrogonatos et al. [35]; it presents further geological and mineralogical data regarding the Konos Hill lithocap and aims to expand previous knowledge on the mineralogy and mineral chemistry of advanced argillic alteration zones in the Sapes district. The study emphasizes in the mineral-chemical implications of phases such as zunyite and APS minerals, because they may constitute an exploration tool for new mineralized centers in the adjacent areas and can be used to define the physicochemical conditions of the transition from the porphyry to the epithermal environment in the Konos Hill prospect.

2. Materials and Methods

Twenty rock samples were collected from the advanced argillic-altered rocks of the Konos Hill area for petrographic, mineralogical, mineral-chemical, and geochemical studies. From these samples, sixteen polished-thin sections underwent detailed petrographical investigation using an Axio Scope.A1 (Zeiss) transmitted light microscope.

Powders from ten representative samples were analyzed by X-ray diffraction, using a Siemens/Bruker 5005 X-ray diffractometer at the Faculty of Geology and Geoenvironment, National and Kapodistrian University of Athens. Results were evaluated using the software package DIFFRACplus, EVA (version 10.0). Alteration assemblages in selected rock chips were also determined using short-wave infrared spectroscopy (SWIR) with a portable TerraSpec 4 Standard-Res mineral analyzer.

The chemical compositions of selected minerals (alunite–natroalunite, APS, diaspore, zunyite) were determined by electron probe microanalysis (EPMA) using a JEOL 8530F instrument at the Institute of Mineralogy, University of Münster, Germany. Analytical conditions included a 15-kV accelerating voltage, a 5-nA beam current, and counting times of 10 s for peaks and 5 s for the background signal. Natural (for Na, Mg, Al, Si, Mn, Fe, Sr, Cl, Ba, K, Ca, P, and S) and synthetic (for F, Ti, Cr, La, Ce, Nd, and Pb) mineral standards were used for calibration prior to quantitative analyses. The phi-rho-z correction was applied to all data. Standard deviations of the major oxides are within 1–2%. Oxides and elements that were analyzed and their average (1σ) detection limits are: Na_2O (0.046 wt %), MgO (0.43 wt %), Al_2O_3 (0.038 wt %), SiO_2 (0.058 wt %), MnO (0.054 wt %), FeO (0.057 wt %), SrO (0.082 wt %), Cl (0.021 wt %), BaO (0.094 wt %), K_2O (0.032 wt %), CaO (0.038 wt %), P_2O_5 (0.049 wt %), SO_3 (0.063 wt %), F (0.14 wt %), TiO_2 (0.13 wt %), La_2O_3 (0.25 wt %), Ce_2O_3 (0.20 wt %), Nd_2O_3 (0.20 wt %), and PbO (0.047 wt %).

In addition, eight mineralized lithocap samples were analyzed commercially by inductively coupled plasma mass spectrometry (ICP-MS package AQ251) at ACME analytical laboratories in Vancouver, BC, Canada, in order to determine their metal concentrations.

3. Geological Setting

3.1. Regional Geology

The Hellenides are part of the Alpine orogenic system and form the link between the Dinarides (e.g., Albania) to the NW and the Pontides in the east (e.g., Turkey). They comprise a SW-vergent succession of tectonic units, which were integrated in three continental blocks (Rhdopes, Pelagonia, External Hellenides/Adria) and two oceanic domains, the Vardar and Pindos, respectively [36,37].

Among these units, lithologies of the Rhodope Massif, located mainly in NE Greece (Figure 1), record a long and rather complex tectonometamorphic history related to terrane accretion, subsequent exhumation of deep-seated crustal rocks along major detachment faults, and formation of metamorphic core complexes [38]. They are divided into three major lithological subdomains: (a) the North Rhodope domain; (b) the Southern Rhodope Core complex (also including the Kerdyllion Unit); and (c) the Chalkidiki block, which consists of the so-called Serbo-Macedonian Massif, with the exception of the Kerdyllion Unit [36]. Core complex formation and associate exhumation of high-grade metamorphic rocks in the Rhodope Massif occurred during two periods. The first (40–35 Ma) is related to the subduction of the Pindos ocean and accretion of the Pelagonian microcontinent to the Eurasian margin [39,40]. The second, at ~35 Ma [41], is related to subduction and accretion of the

External Hellenides continental block with contemporaneous inception of subduction in the Mediterranean ocean.

The North Rhodope domain consists of (a) a lower high-grade unit of basement rocks, including the metamorphic core complexes of Arda, Biala Reka-Kechros, and Kesebir-Kardamos; (b) an intermediate unit comprising high-grade basement rocks; and (c) an upper unit consisting of low-grade metamorphic sequences of the Circum-Rhodope belt and ophiolitic rocks [42]. The Southern Rhodope Core Complex comprises Paleozoic orthogneisses (possibly equivalent to those of the metamorphic core complexes of the North Rhodope domain [37]) and a thick succession of Triassic marbles, with intercalations of amphibolitic and metapelitic rocks. Locally, anatectic conditions were achieved, as evidenced by migmatites on Thasos island and within the Kerdyllion unit. Finally, the Chalkidiki block represents a thrust system composed of NW-trending units, comprising various lithologies including ophiolitic rocks.

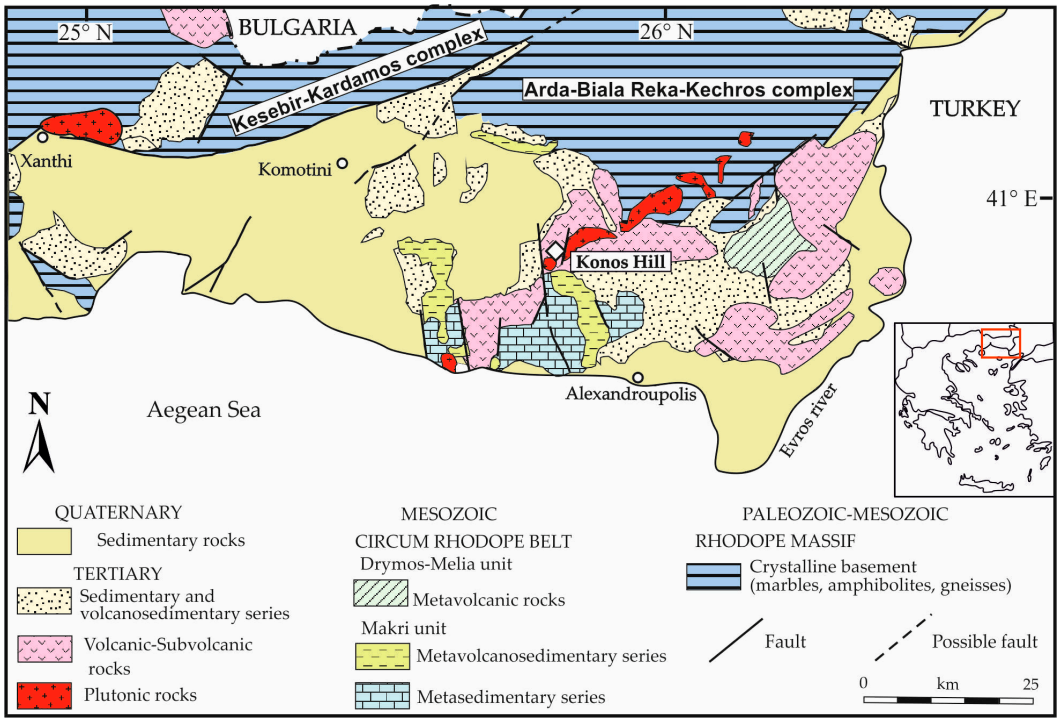

Figure 1. Geological map of NE Greece (modified from [22]). The white diamond marks the location of the study area.

Lithologies of the Rhodope were exhumed during a late Cretaceous to Tertiary, syn- to postorogenic collapse. The deep-seated metamorphic successions were uplifted along major detachment faults, resulting in the formation of metamorphic core complexes and the opening of several E–W-trending, structurally controlled basins [43,44]. Syn-extensional sedimentation, which lasted from the upper Eocene to Miocene, resulted in the deposition of extensive sequences of transgressive conglomerates, limestones, and sandstones [45]. During the orogenic collapse, contemporaneous asthenospheric upwelling due to crustal thinning gave rise to widespread late Eocene to Miocene, postsubduction magmatism. Igneous rocks formed outcrops extensively in the Rhodope and Serbo-Macedonian domains [46]. Magmatic rocks have calc-alkaline to shoshonitic and ultrapotassic affinities, and have mafic to felsic compositions [46,47]. In many cases, magmatism was followed by intense hydrothermal alteration, which lead to the formation of abundant mineral deposits, mainly in the Rhodopic, and to a lesser extent, the Serbo-Macedonian domains [43,48].

3.2. Local Geology

In the Kassiteres–Sapes district, lithologies of the Circum-Rhodope Belt crop out, especially in its southern part. Metasedimentary lithologies of the Makri unit are most widespread (Figure 1).

Eocene volcanosedimentary rocks discordantly overlie the metamorphic basement and occupy most of the study area.

The Konos Hill area is part of a deeply eroded volcanic edifice built on the Eocene sedimentary deposits [23]. This volcanic edifice comprises mostly subvolcanic intrusions of calc-alkaline to high-K calc-alkaline affinities, as well as lava domes, flows, and pyroclastic rocks. Both magmatic and pyroclastic rocks are characterized by intense hydrothermal alteration.

Konos Hill, its most prominent topographic feature, is located approximately 20 km N–NW of Alexandroupolis and consists of a hydrothermally altered granodiorite which intruded the volcanosedimentary rocks (Figure 2). Further to the ENE in the study area, a monzodioritic body intruded the volcanosedimentary rocks and the granodiorite. Available geochronological data for the monzodiorite yielded cooling ages of 31.9 ± 0.5 Ma (Rb/Sr on biotite [49]) and 32.6 ± 0.5 Ma ($^{40}Ar/^{39}Ar$ on biotite [50]). Recently, Perkins et al. [51] conducted a U–Pb zircon geochronological study on the Kassiteres magmatic suite, showing that magmatism occurred between 32.05 ± 0.02 and 32.93 ± 0.02 Ma. Previous studies in this area have shown that the granodiorite hosts the Konos Hill porphyry Mo–Cu–Re–Au porphyry prospect [22,26,27].

Major faults in the Konos Hill area strike N–S, NNE–SSW, and E–W (Figure 2) and are usually high-angle faults (dipping between 60–80°). Zones of advanced argillic alteration mostly trend E–W and are related to the previously mentioned fault directions, indicating that magma emplacement, hydrothermal alteration, and associated mineralization were structurally controlled.

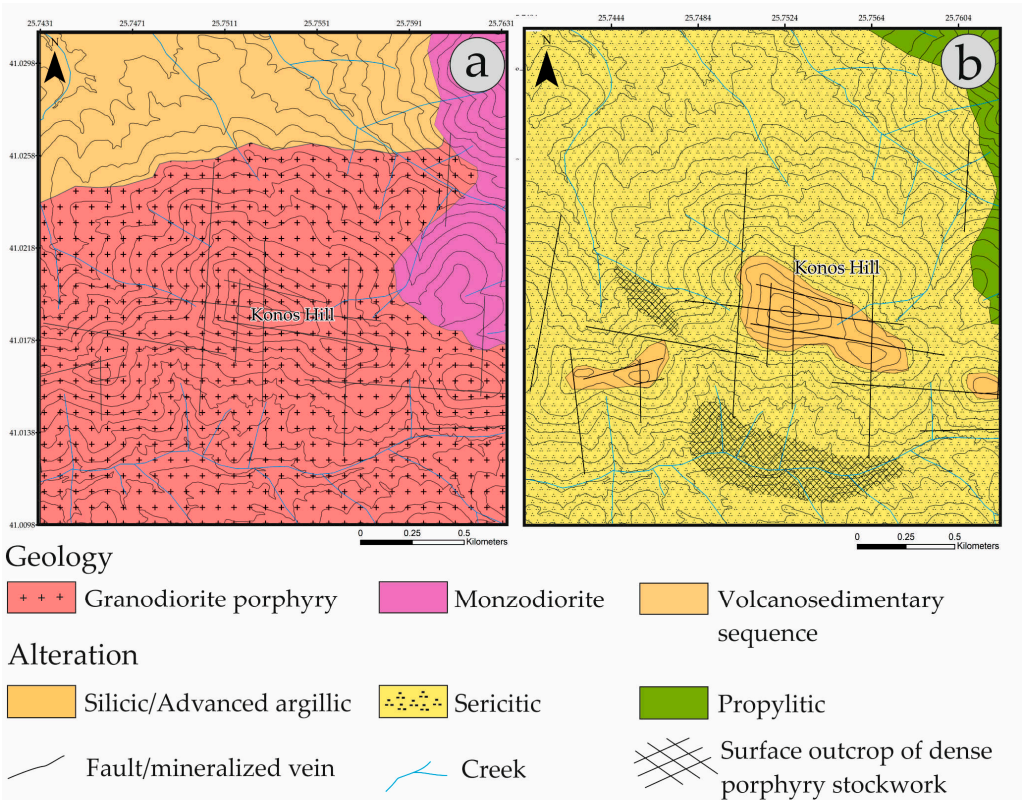

Figure 2. Geological (**a**) and alteration (**b**) map of the Konos Hill area, NE Greece (modified after Mavrogonatos et al., [35]).

4. Results and Discussion

4.1. Alteration and Mineralization

Hydrothermal alteration and mineralization occurring in the Kassiteres–Sapes district have been well-studied [23–26,35,52–54]. Advanced argillic-altered lithocaps have been recognized at a number of sites [23]. Among them, Konos Hill is located in the eastern part of the district and comprises the highest topographic level of the area.

Advanced argillic alteration at Konos Hill is related to E–W, N–S, and NNW–SSE trending fault lines. The latter direction is also related to porphyry-style stockwork outcrops, which are best exposed at lower elevation (Figure 3a). In the uppermost part, acidic leaching of the granodiorite resulted in a structurally controlled and spatially restricted zone, which comprises residual quartz with a vuggy texture. This zone grades outwards and downwards into alunite-rich assemblages (Figure 3b–e), which comprise alunite + APS minerals + quartz + zunyite ± pyrophyllite and quartz + alunite + APS minerals + diaspore + kaolinite ± pyrophyllite. Hematite pseudomorphs after pyrite accompany the abovementioned assemblages. The Konos Hill lithocap is deficient of any primary sulfides due to extensive supergene oxidation; however, it hosts a low-grade Au mineralization (see Section 4.3). On the contrary, nearby lithocaps at Agios Demetrios, Scarp, Viper, and Agia Barbara host significant high-sulfidation epithermal, gold–enargite mineralization, which is generally found in the western part of the study area [22–25,55–57]. Advanced argillic alteration assemblages evolve downwards through a transitional zone of quartz + alunite + pyrophyllite + sericite into a typical sericite-rich assemblage, which is the most widespread type of hydrothermal alteration in the district. The latter hosts porphyry-style (A- and banded) quartz stockwork (Figures 3f and 4i) and D-type quartz–sericite veins with a pyrite–molybdenite–chalcopyrite–rheniite mineralization [22,26,27]. Minor amounts of enargite, colusite, tetrahedrite–tennantite group minerals, and galena occur both within the veins and as disseminations in the sericitic-altered granodiorite and comprise a high-sulfidation mineralization superimposed on the porphyry system.

Extensive sericitic alteration also affected outcrops of the volcanosedimentary succession as well as parts of the monzodiorite intrusion, especially along fault planes. It grades further outwards into propylitic alteration that is characterized by varying amounts of epidote, chlorite, and carbonates.

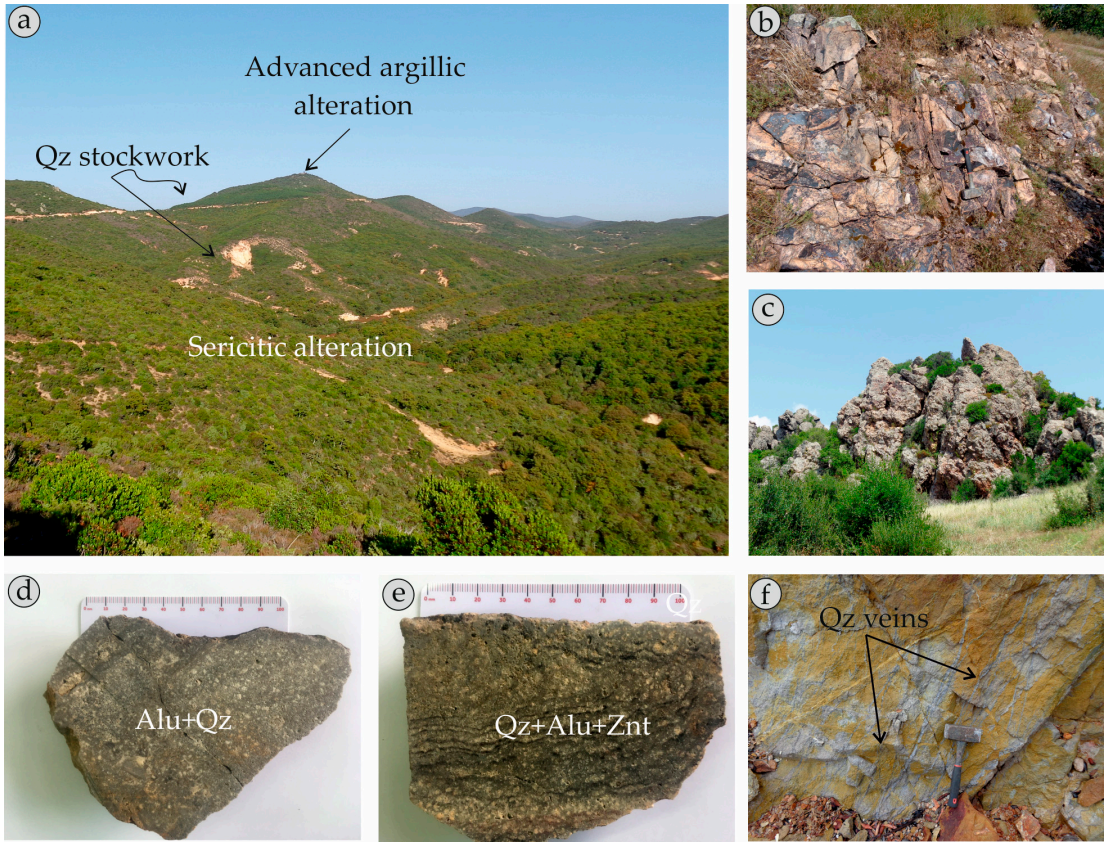

Figure 3. Field and hand-specimen photographs from Konos Hill, NE Greece. (**a**) Panoramic view of Konos Hill; (**b**) Quartz–alunite–zunyite-bearing rocks on top of Konos Hill; (**c**) Quartz–alunite–diaspore-bearing rocks in the NW slopes of Konos Hill; (**d**,**e**) Hand-specimens of quartz–alunite (Alu + Qz) and quartz–alunite–zunyite (Qz + Alu + Znt) assemblages; (**f**) Quartz porphyry stockwork veins in sericitic-altered granodiorite from Saporema Creek.

4.2. Mineralogy and Mineral Chemistry

4.2.1. Zunyite

Zunyite forms euhedral crystals that are up to 300 μm in size (Figures 4a,b and 5a). They are commonly associated with quartz and tabular alunite–natroalunite crystals, with minor amounts of spheroidal hematite, which along with goethite, formed after pyrite (Figure 4a,b). In rare cases, zunyite contains submicroscopic APS inclusions (Figure 5b). Electron probe microanalyses show significant compositional variations (Table 1). The SiO_2 varies from 22.7 to 25.14 wt %, whereas the Al_2O_3 content clusters tightly at 54.97 to 55.81 wt %. Fluorine and chlorine contents range between 4.07 and 5.93 wt % and 2.72 to 2.97 wt %, respectively. In some cases, traces of Na_2O, BaO, TiO_2, Na_2O, Ce_2O_3, and Nd_2O_3 were detected (up to 0.40, 0.26, 0.23, 0.34, and 0.21 wt %, respectively).

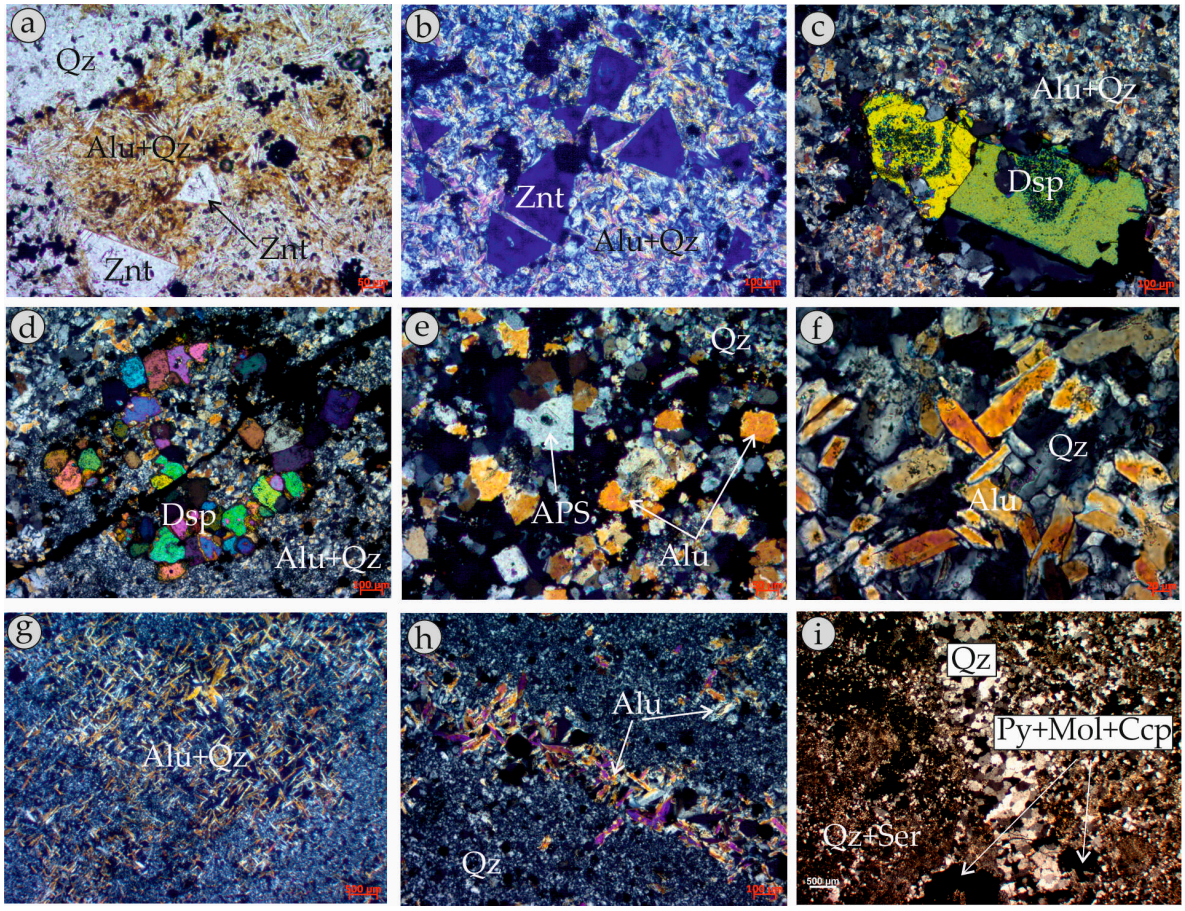

Figure 4. Transmitted light microphotographs of alteration assemblages from the Konos Hill area, NE Greece. (**a**,**b**) Euhedral zunyite (Znt) crystals in association with quartz and tabular alunite (Alu + Qz, plane-polarized and crossed-polarized light, respectively); (**c**) Subhedral diaspore (Dsp) crystals displaying concentric zonation patterns (crossed polarized light); (**d**) Subhedral diaspore (Dsp) crystals set in an alunite (Alu) and quartz (Qz) matrix of altered granodiorite (crossed-polarized light); (**e**) APS crystals form the core of pseudocubic alunite (crossed-polarized light); (**f**) Tabular alunite crystals in association with quartz (Qz, crossed-polarized light); (**g**) Alunite (Alu) aggregate replacing a phenocryst in the granodiorite (crossed-polarized light); (**h**) Alunite (Alu) crystals forming veinlets in the quartz (Qz)-dominated matrix (crossed-polarized light); (**i**) Sugary quartz (Qz) crystals in porphyry-style vein hosting pyrite–molybdenite–chalcopyrite ore (Py + Mol + Ccp) in sericite-altered granodiorite (crossed-polarized light).

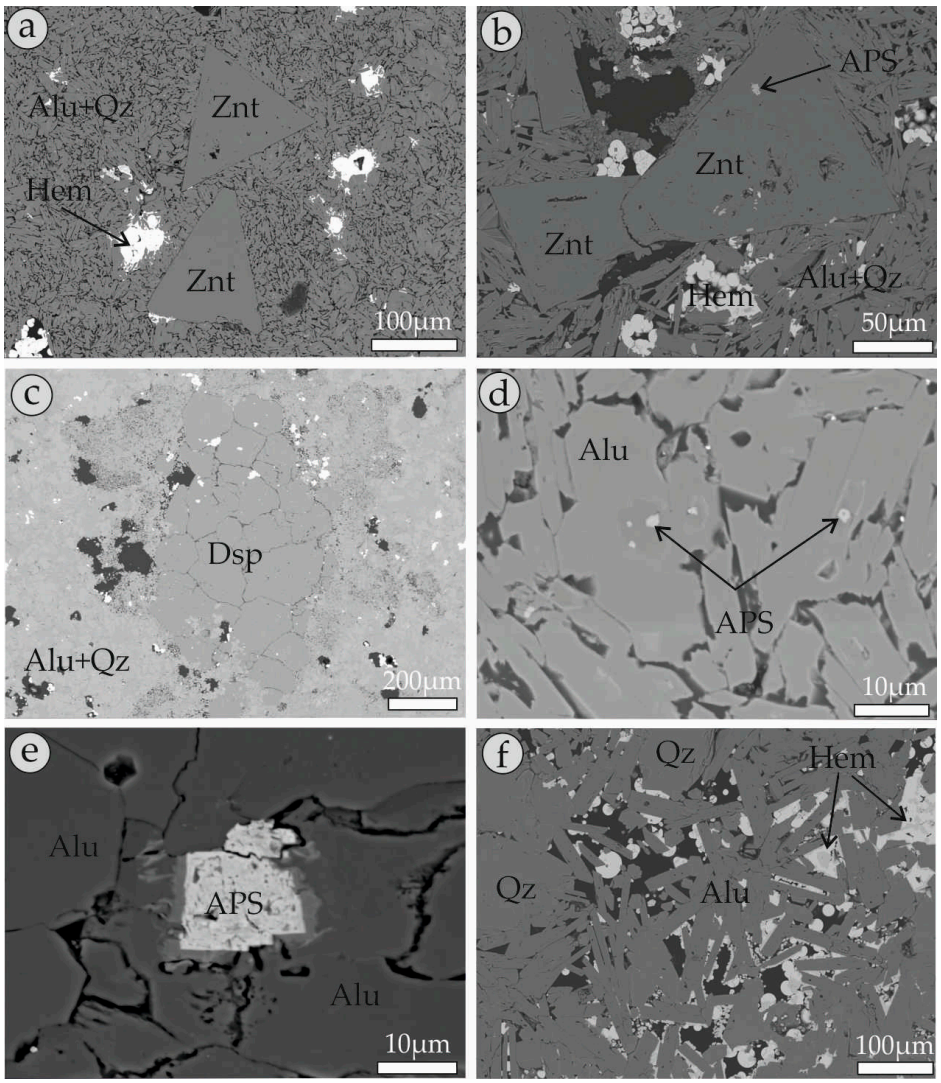

Figure 5. Back-scattered electron images of alteration minerals contained in samples from Konos Hill, NE Greece: (**a**) Euhedral zunyite (Znt) crystals in association with quartz, tabular alunite (Alu + Qz), and hematite (Hem); (**b**) APS included in euhedral zunyite (Znt); (**c**) Diaspore (Dsp) crystals included in an alunite and quartz (Alu + Qz)-dominated matrix; (**d**,**e**) APS pseudocubic crystals in the core of tabular-shaped alunite; (**f**) Tabular alunite (Alu) in association with quartz (Qtz) and hematite (Hem).

Table 1. Representative EPMA data of zunyite (1–6) and diaspore (7–10) from the advanced argillic alteration zone of the Konos Hill prospect, NE Greece.

wt %	1	2	3	4	5	6	7	8	9	10
SiO_2	25.14	22.96	23.66	24.35	22.70	24.58	bd	bd	bd	bd
TiO_2	bd	0.11	bd	0.26	bd	bd	0.18	bd	bd	bd
Al_2O_3	55.03	54.97	55.25	54.76	55.81	55.32	83.05	82.58	82.42	82.57
FeO	bd	0.05	0.04	0.16	bd	0.08	bd	bd	bd	bd
Na_2O	0.40	0.11	0.34	0.09	0.39	0.19	0.02	bd	0.02	0.01
BaO	0.11	bd	bd	bd	bd	0.23	0.98	bd	bd	bd
La_2O_3	bd	bd	bd	bd	bd	bd	bd	bd	bd	0.34
Ce_2O_3	bd	bd	bd	bd	bd	0.34	bd	0.38	0.24	bd
Nd_2O_3	bd	bd	0.21	bd	bd	bd	bd	0.30	0.16	0.22
P_2O_5	0.05	0.51	0.27	0.25	0.70	0.11	0.05	bd	0.05	bd
F	5.93	4.56	4.82	4.07	5.08	4.32	bd	0.11	bd	bd
Cl	2.90	2.82	2.97	2.91	2.72	2.75	bd	bd	0.01	bd
Total	89.63	86.16	87.60	86.92	87.47	88.04	84.42	83.37	82.90	83.23
apfu	29.5 (O)						1.5 (O)			
Si	5.013	4.679	4.787	4.895	4.596	4.920	0.000	0.000	0.000	0.000
Ti	0.005	0.017	0.000	0.039	0.000	0.000	0.001	0.000	0.000	0.000
Al	12.931	13.202	13.150	12.976	13.190	12.919	0.994	0.997	0.997	0.996

Fe	0.000	0.009	0.007	0.027	0.000	0.013	0.000	0.000	0.000	0.000
Na	0.016	0.043	0.134	0.033	0.154	0.072	0.000	0.000	0.000	0.000
Ba	0.001	0.005	0.002	0.001	0.000	0.018	0.004	0.000	0.000	0.000
La	0.002	0.000	0.000	0.000	0.000	0.002	0.000	0.000	0.000	0.002
Ce	0.000	0.011	0.002	0.003	0.000	0.027	0.000	0.000	0.001	0.001
Nd	0.000	0.000	0.015	0.000	0.000	0.000	0.001	0.001	0.001	0.001
P	0.008	0.089	0.046	0.043	0.120	0.019	0.000	0.000	0.001	0.000
F	3.224	2.956	2.704	2.305	2.837	2.431	0.000	0.004	0.000	0.000
Cl	0.844	0.860	0.891	0.884	0.817	0.830	0.000	0.000	0.000	0.000

bd: below detection; apfu: atoms per formula unit.

4.2.2. Diaspore

Diaspore is generally found as euhedral to subhedral crystals measuring up to 0.2 cm in size. Commonly, it forms isolated grains scattered in a fine-grained matrix of tabular alunite crystals and quartz (Figure 4c). Diaspore also forms aggregates of fine-grained subhedral crystals that replace earlier mineral phases of the silicified rock such as feldspars (Figures 4d and 5c). In some cases, diaspore crystals occur as euhedral grains in fissures or cracks in the matrix. Electron microprobe analyses reveal near stoichiometric compositions with traces of TiO_2, BaO, and REE, mostly Ce_2O_3 and Nd_2O_3 (up to 0.18, 0.98, 0.38, and 0.22 wt %, respectively; Table 1). Concentric zoning patterns occur in some crystals (Figure 4c), but are apparently not associated with chemical variations.

4.2.3. Alunite Supergroup Minerals

Alunite supergroup minerals consist of four major subgroups, each one containing a varying number of different members. These subgroups consist of the alunite (e.g., alunite, natroalunite), beudantite (e.g., woodhouseite, svanbergite), plumbogummite (e.g., crandalite, florencite), and dussertite groups (e.g., arsenocrandalite, segnitite) [58–61]. Microscopic examinations together with EPMA data reveal a wide compositional range for alunite supergroup minerals in the Konos Hill area. Based on in the distribution of data in Figure 6a, analyzed compositions comprise members of the alunite, beudantite, and plumbogummite subgroups.

Aluminum phosphate–sulfate (APS) minerals occur mostly as euhedral pseudocubic inclusions in zoned natroalunite in all types of advanced argillic assemblages at Konos Hill (Figures 4e and 5d,e). EPMA data (Table 2) revealed varying amounts of CaO (up to 10.96 wt %), BaO (up to 3.60 wt %), SrO (up to 9.54 wt %), Ce_2O_3 (up to 11.06 wt %), La_2O_3 (up to 4.90 wt %), Nd_2O_3 (up to 4.72 wt %), and P_2O_5 (up to 29.55 wt %). In many cases, minor concentrations of K_2O and Na_2O were detected (up to 0.99 and 0.83 wt %, respectively). It is notable that all analyzed APS minerals contained small amounts of fluorine (up to 1 wt %). Chemical variations of the APS minerals are summarized in Table 2 and shown in Figure 6a–d. The most common compositions include woodhouseite and svanbergite. Crandallite and florencite are rare. Woodhouseite is the most common APS and it was present with near end-member compositions, although Ba- and Sr-rich varieties were also identified. The average compositions of woodhouseite and svanbergite correspond to the formulae $Ca_{0.63}Ba_{0.05}Na_{0.06}Sr_{0.20}Ce_{0.02}Al_{3.07}(SO_4)_{0.87}(PO_4)_{1.17}$ and $Sr_{0.37}Ca_{0.20}Ba_{0.07}Ce_{0.03}Al_{3.08}(SO_4)_{0.87}(PO_4)_{1.16}$, respectively. Crandallite is usually Sr-rich, whereas florencite–(Ce) was also identified (Table 2).

The APS minerals studied here comprise solid solution members of the beudantite and plumbogummite subgroups. They plot along the 1:1 line in Figure 6a and display a progressive substitution of PO_4^{3-} by SO_4^{2-}, coupled with a substitution of monovalent (K, Na) by divalent (Ca, Ba, Sr) cations in the D site. Compositions that plot further below this line display a significant variation in P, whereas compositional variations in the D site are limited. This points towards protonation of one of their trivalent anions to establish charge balance. Moreover, the APS minerals that are devoid of monovalent cations (P > 1 apfu) are also characterized by a 1:1 substitution in the monovalent-bearing D site by divalent cations (Figure 6b), whereas compositions that plot below this line indicate significant vacancies due to charge balance. In addition, APS compositions that exhibit elevated phosphate contents are, according to Scott [62], consistent with the appearance of trivalent cations substituting in the A site of the minerals. This is mirrored by the presence of Ce-rich varieties such as florencite–(Ce) in Konos Hill. This substitution is in agreement with the findings of Voudouris [23]

and Voudouris and Melfos [29], who studied the APS mineralogy of the Kassiteres–Sapes and Melitena prospects, respectively.

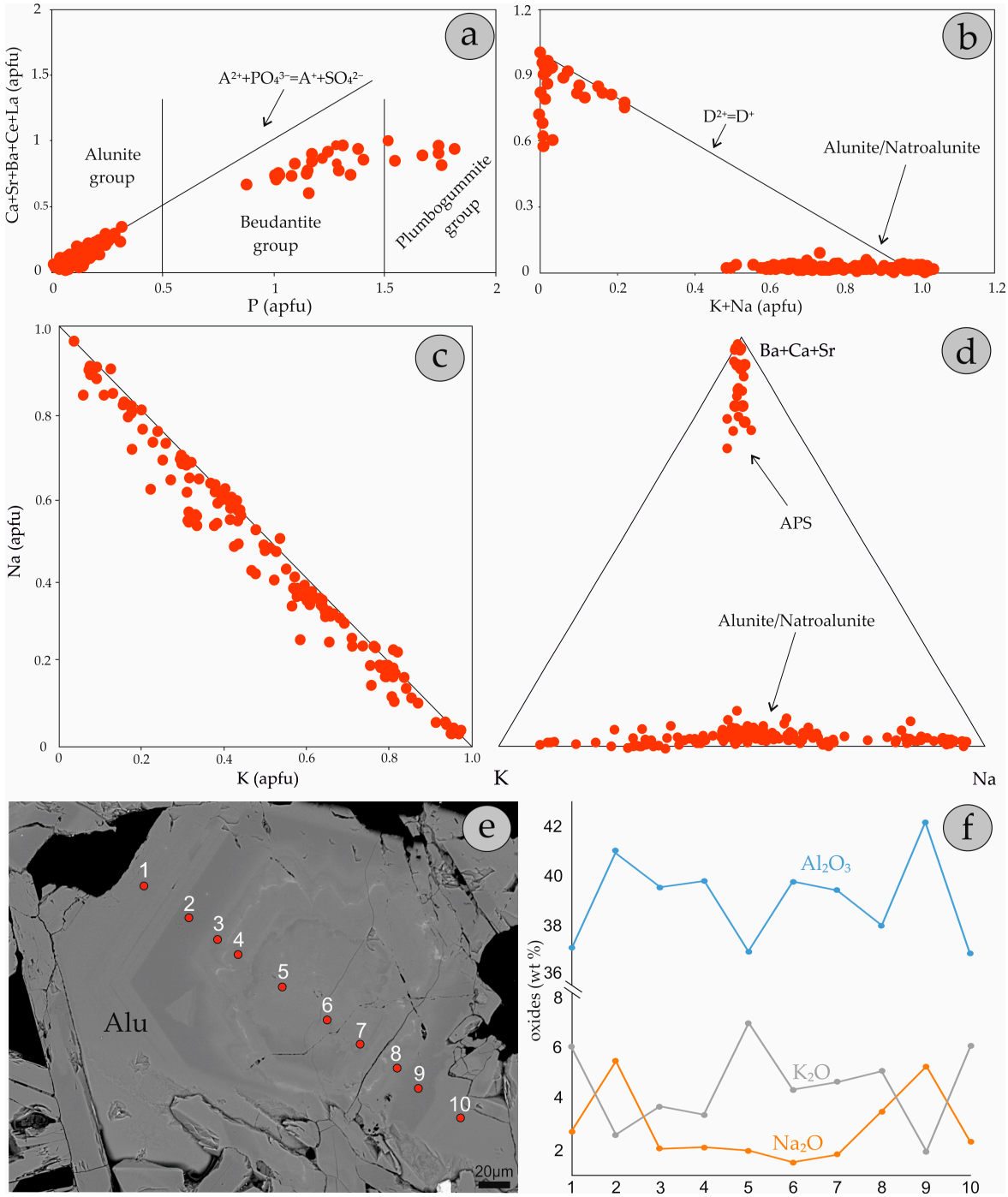

Figure 6. Chemical variation diagrams of alunite and APS minerals from the Konos Hill area, NE Greece. (**a**) Ca + Sr + Ba + Ce + La vs. P plot (the line represents the occupancy of divalent and trivalent cations in the A site relative to trivalent anions in the X site); (**b**) Ca + Sr + Ba + Ce + La vs. K + Na plot (the line represents the occupancy of monovalent relative to divalent cations in the D site); (**c**) Na vs. K in A sites; (**d**) Ternary K–Na–(Sr + Ba + Ca) plot of alunite supergroup minerals; (**e**) Back-scattered electron image showing a zoned alunite crystal. Numbers indicate EPMA analytical spots; (**f**) Profile depicting the chemical variations of alunite in terms of Al_2O_3, Na_2O, and K_2O (wt %). Numbers on the *x* axis represent the analyzed spots shown in (**e**).

Table 2. Representative EPMA data of APS minerals from the advanced argillic alteration zone of the Konos Hill prospect, NE Greece. 1: Ba–rich woodhouseite; 2–4: Ca–rich svanbergite; 5: Ce–Ba–Ca–rich svanbergite; 3,7,8: Sr–rich woodhouseite; 6: Ba–rich svanbergite; 9: Sr–rich crandalite; 10: florencite–(Ce).

wt %	1	2	3	4	5	6	7	8	9	10
Al_2O_3	33.59	34.10	34.22	35.41	36.67	34.88	34.48	38.09	32.79	32.31
FeO	0.09	0.06	bd	bd	0.10	bd	bd	bd	bd	0.07
CaO	10.96	3.36	7.11	3.93	2.11	0.97	5.86	5.91	5.94	0.66
Na_2O	0.61	0.28	0.08	0.31	0.48	0.27	0.36	0.83	0.12	bd
K_2O	0.48	0.37	0.21	0.59	0.99	0.78	0.74	0.89	0.43	0.11
BaO	1.47	1.52	0.87	1.61	2.10	3.60	1.09	1.06	0.97	3.92
La_2O_3	0.50	0.07	bd	0.19	0.43	0.91	bd	bd	bd	4.90
Ce_2O_3	1.42	0.32	bd	0.88	2.48	2.53	1.14	bd	bd	11.06
NdO_3	0.10	0.34	bd	0.10	1.45	3.48	0.30	bd	bd	4.72
SrO	0.83	9.54	7.63	8.41	7.45	6.33	5.37	4.54	7.82	3.30
PbO	bd	bd	bd	0.05	0.05	bd	bd	0.22	bd	bd
SO_3	15.33	14.35	11.81	15.95	14.98	14.32	13.63	20.31	3.19	3.63
P_2O_5	16.72	17.35	21.57	18.26	19.27	18.53	20.26	15.58	29.55	23.03
F	0.49	0.97	0.51	0.25	0.98	0.17	0.67	0.83	0.56	0.41
Total	82.59	82.63	84.10	85.94	89.54	86.83	83.92	88.35	81.41	88.12
apfu					11 (O)					
Al	3.022	3.034	3.037	3.098	3.067	3.139	3.060	3.180	2.996	3.076
Fe	0.007	0.004	0.000	0.000	0.006	0.000	0.001	0.000	0.000	0.005
Ca	0.858	0.282	0.574	0.313	0.161	0.080	0.473	0.445	0.488	0.057
Na	0.096	0.042	0.011	0.045	0.067	0.040	0.052	0.113	0.012	0.000
K	0.053	0.036	0.019	0.056	0.090	0.076	0.071	0.081	0.04	0.011
Ba	0.047	0.046	0.027	0.047	0.058	0.108	0.032	0.029	0.029	0.119
La	0.015	0.002	0.000	0.005	0.011	0.025	0.000	0.002	0.000	0.146
Ce	0.042	0.010	0.000	0.024	0.006	0.071	0.031	0.000	0.000	0.528
Nd	0.003	0.010	0.000	0.003	0.037	0.095	0.008	0.000	0.000	0.136
Sr	0.028	0.433	0.333	0.362	0.306	0.280	0.235	0.186	0.340	0.155
Pb	0.000	0.000	0.000	0.001	0.001	0.001	0.000	0.004	0.000	0.000
S	0.934	0.841	0.678	0.888	0.904	0.821	0.770	1.080	0.199	0.221
P	1.081	1.148	1.376	1.147	1.158	1.198	1.292	0.985	1.822	1.741
F	0.121	0.239	0.120	0.058	0.216	0.042	0.156	0.113	0.129	0.106

bd: below detection; apfu: atoms per formula unit.

Alunite and natroalunite are the most common representatives of the supergroup and are found as minor constituents in the vuggy silica in both quartz + zunyite + kaolinite ± pyrophyllite and quartz + diaspore + kaolinite ± pyrophyllite assemblages, as well as in the transitional zone to the sericitic alteration. They are generally found in tabular-shaped or rhombohedral crystals that replaced earlier formed phenocrysts (e.g., feldspars, Figure 4g) or mafic minerals in the host rocks. However, pseudocubic shapes were also observed (Figures 4e–h and 5). In other cases, tabular alunite forms in small veinlets crosscutting the silicified matrix. Many alunites are K-rich, with K_2O values reaching up to almost 9 wt % (Table 3). This corresponds to an average chemical formula of $K_{0.39}Na_{0.30}Ca_{0.01}Ba_{0.01}Al_{3.06}(SO4)_{1.96}(PO4)_{0.01}$. Sodium-rich alunite is more common and usually forms euhedral, tabular-shaped crystals with sizes up to 500 μm. In this case, the Na_2O content is higher than K_2O and reaches up to 5.51 wt %, corresponding to the average formula $Na_{0.61}K_{0.35}Ca_{0.01}Al_{3.01}(SO4)_{1.98}(PO4)_{0.01}$. Substitution between Na and K in the D sites of alunite is almost ideal, leading to complete substitution of K by Na (Figure 6c). However, the majority of the analyzed compositions deviate from the ideal 1:1 substitution, probably reflecting vacancies in the structure, as proposed by Scott [62] and in accordance with the findings of Voudouris [23]. Moreover, a few analyses plot above the 1:1 line and probably reflect a partial excess of K or Na in the D sites. Many grains of alunite carry traces of CaO, FeO, SrO, BaO, La_2O_3, Ce_2O_3, and Nd_2O_3 (values up to 0.38, 0.46, 0.38, 0.75, 0.42, 0.36, and 0.33 wt %, respectively). In some cases, oscillatory zoning is present in alunite crystals, as shown by alternations of concentric K- and Na-rich bands in Figure 6e,f. Many alunite grains, especially the tabular-shaped, zoned natroalunite, include cores of APS minerals, mostly woodhouseite or svanbergite.

Table 3. Representative EPMA data of members of the alunite–natroalunite solid solution from the advanced argillic alteration zone at the Konos Hill prospect, NE Greece.

wt %	1	2	3	4	5	6	7	8	9	10	11	12	13	14	15
Al_2O_3	37.90	37.66	39.47	36.54	37.19	37.40	37.65	36.80	36.96	38.08	42,41	36.95	38.24	40.44	39.95
FeO	0.46	0.30	0.23	0.12	0.28	0.17	0.02	0.10	0.07	bd	0.01	bd	bd	bd	0.12
CaO	0.01	0.02	0.05	0.38	0.03	0.07	0.02	bd	bd	0.09	0.10	0.01	0.05	0.00	0.05
Na_2O	4.63	5.12	2.57	3.07	4.58	5.01	2.79	1.78	1.97	5.51	5.31	1.97	1.64	1.33	2.18
K_2O	3.52	3.59	3.02	4.91	3.90	3.41	5.75	7.10	6.86	2.6	1.95	7.02	4.71	4.44	3.69
BaO	0.15	0.37	0.21	0.21	0.10	0.21	0.16	bd	0.12	0.11	0.17	0.46	0.75	0.30	0.38
SrO	bd	bd	0.28	0.38	0.12	bd	0.19	bd	bd	0.15	0.22	0.05	0.24	bd	0.07
La_2O_3	bd	bd	bd	bd	0.37	0.25	0.26	bd	bd	bd	0.19	0.25	bd	0.42	bd
Ce_2O_3	0.11	bd	0.35	bd	0.13	0.11	bd	bd	0.19	bd	bd	0.36	bd	bd	0.15
Nd_2O_3	bd	bd	bd	0.28	bd	bd	0.33	bd	bd	bd	bd	0.27	0.25	0.11	bd
SO_3	34.74	35.16	36.72	34.05	34.24	34.57	34.73	33.69	34.52	34.46	35.48	33.66	33.93	36.46	35.05
Total	81.61	82.32	82.90	79.97	80.94	81.28	81.90	79.49	80.69	81.00	85.81	81.01	79.89	83.52	81.64
apfu								11 (O)							
Al	3.218	3.177	3.238	3.106	3.198	3.190	3.218	3.231	3.302	3.241	3.391	3.229	3.223	3.309	3.391
Fe	0.028	0.018	0.014	0.01	0.017	0.01	0.000	0.006	0.004	0.000	0.000	0.000	0.000	0.000	0.007
Ca	0.001	0.001	0.004	0.029	0.002	0.005	0.001	0.000	0.000	0.007	0.007	0.001	0.004	0.000	0.004
Na	0.646	0.708	0.317	0.335	0.649	0.704	0.392	0.258	0.279	0.772	0.701	0.283	0.228	0.181	0.296
K	0.324	0.332	0.298	0.447	0.363	0.315	0.532	0.675	0.644	0.240	0.169	0.664	0.430	0.400	0.331
Ba	0.004	0.010	0.006	0.006	0.002	0.004	0.004	0.000	0.003	0.004	0.004	0.013	0.021	0.008	0.010
Sr	0.000	0.000	0.011	0.006	0.006	0.000	0.008	0.000	0.000	0.005	0.009	0.002	0.010	0.000	0.003
La	0.000	0.000	0.000	0.000	0.022	0.007	0.007	0.000	0.000	0.000	0.005	0.007	0.002	0.011	0.000
Ce	0.003	0.000	0.012	0.000	0.010	0.003	0.000	0.000	0.005	0.000	0.001	0.010	0.000	0.001	0.004
Nd	0.000	0.000	0.000	0.000	0.003	0.000	0.009	0.000	0.000	0.000	0.000	0.007	0.007	0.003	0.000
S	1.878	1.889	1.789	1.716	1.879	1.891	1.890	1.894	1.904	1.868	1.816	1.873	1.738	1.855	1.847

bd: below detection; apfu: atoms per formula unit.

4.2.4. Kaolinite–Pyrophyllite

Kaolinite and pyrophyllite are present as minor constituents and usually form small, acicular aggregates that accompany quartz–alunite–APS–diaspore and quartz–alunite–zunyite–APS assemblages. Their presence, in addition to microscopic examination, was verified by X-ray diffraction and SWIR investigations.

4.3. Bulk Ore Geochemistry

Bulk analyses of advanced argillic-altered samples reveal (Table 4) low concentration values of Au and Ag, which reach up to 0.36 and 0.22 ppm, respectively. Pb concentration values reach up to 122 ppm, while a relative enrichment is also remarked in chalcophile elements such as Mo (up to 19 ppm), Bi (up to 13 ppm), and Se (up to 26 ppm), which mirrors the close genetic relation of the lithocap to the underlying porphyry-style mineralization. Finally, Ga and Sn are also enriched, with values up to 17 and 18 ppm, respectively.

Table 4. Metallic element concentrations of samples from the high-sulfidation mineralization at the Konos Hill prospect, NE Greece (values in ppm).

Sample	1	2	3	4	5	6	7	8
As	15	18	34	18	4	6	67	66
Ag	0.19	0.16	0.13	0.23	0.22	0.04	0.12	0.13
Au	0.04	0.02	0.36	0.19	0.04	0.03	bd	0.05
Cu	10	7	7	5	32	9	14	13
Bi	2.03	2.97	2.42	2.08	6.79	1.79	13	9.22
Mo	3.56	2.36	2.37	3.76	19	5.95	1.30	4.55
Se	2.50	4.40	14	5.90	26	6.50	2.50	11
Te	0.23	0.12	0.16	0.21	0.71	0.16	0.78	1.83
Pb	110	116	122	93	169	59	93	87
Zn	4.40	2.50	2	4.30	5.80	7.40	12	6.60
Sb	5.07	1.88	1.93	5.34	4.89	0.56	4.91	7.35
Ga	5.12	4.22	6.72	11	14	17	17	16
Sn	3.70	2.10	2	1.60	4.60	18	1	2.50

bd: below detection; Au detection limit: 0.02 ppm.

4.4. Genetic Implications

Advanced argillic lithocaps form in higher topographic levels from the condensation of magmatic vapors into surface waters, and slightly postdate the potassic alteration in the porphyry environment and the advanced argillic alteration in the high sulphidation environment [8,63]. Field and mineralogical data from the Konos Hill area are consistent with the concept of hypogene formation of the advanced argillic alteration. This is in agreement with the findings of Voudouris [23] and Voudouris and Melfos [29], who described similar assemblages from advanced argillic-altered rocks in the Kassiteres–Sapes and Melitena districts, respectively. The occurrence of both advanced argillic and transitional to sericitic alteration zones in the Konos Hill area is similar to other porphyry/epithermal transitional systems (e.g., Lepanto-Far Southeast, Philippines [5]; Asarel porphyry Cu deposit, Bulgaria [64]), and is the result of different degrees of hydrolytic alteration of the host rocks.

The presence of zunyite in the Konos Hill lithocap [35] reflects the availability of F and Cl in the hydrothermal fluid and can be used to constrain the conditions of formation of the studied assemblages. Estimations can be made based on similar advanced argillic alteration assemblages reported in the literature. A low-temperature limit is set by the coexistence of zunyite with pyrophyllite, which according to Reyes [65,66], is not stabilized at temperatures below 200 °C. Based on isotopic and microthermometric data, Watanabe et al. [10] reported formation temperatures of 260 to 350 °C for an assemblage of zunyite + topaz + diaspore + pyrophyllite in the Kobui area of

Hokkaido, Japan. A similar temperature range (~250 to 380 °C) was reported for the assemblage of topaz + alunite + diaspore + APS + pyrophyllite from the Koryphes Hill area, where topaz, not zunyite, is the F-carrier [24]. Based on similarities between the studied occurrence and the Hugo Dummett porphyry Cu–Au deposit, a T range of 280–350 °C is likely, based on the data of Khasgherel et al. [15]. Further constraints can be made since alunite at Konos Hill contains APS minerals, which according to Hedenquist et al. [5] are formed in a high-temperature environment at the margins of a magmatic intrusion, compared to APS-free alunite. Chemical zonation in the alunite supergroup minerals in the current study, according to Stoffregen and Alpers [12], reflects fast changes in the physicochemical variations in the hydrothermal fluid (decrease in pH and temperature). In addition, the widespread presence of Na-rich alunite versus its K-rich counterpart may suggest either higher temperatures of formation or a higher concentration of Na during the formation of the assemblages. This hypothesis is in accordance with the findings of Chang et al. [67], who stated that high Na/(Na + K) ratios in alunites from the Mankayan area in the Philippines mark the proximity of the assemblage to the intrusive body. In addition, the chemical composition (e.g., Sr/Pb and La/Pb ratios) of alunite can be used as exploration tools, since Pb is highly soluble in higher temperatures and is preferably incorporated in the alunite structure in distal assemblages, where the hydrothermal fluid is cooler, as is the case for the Mankayan deposit [67]. However, at the Melitena prospect, Pb-rich APS minerals are associated with the porphyry-style mineralization [29]. The studied alunites from the Konos Hill prospect are Pb-free, similarly to alunites from the broader Kassiteres–Sapes district [23], thus precluding any application of Pb as an exploration tool, according to Chang et al. [67]. In contrast, the elevated concentrations of Sr and REE in the studied alunite supergroup minerals, as expressed by the presence of woodhouseite and REE-bearing APS minerals (e.g., florencite–Ce) suggest the proximity to the causative intrusion and could be used as an exploration tool in the study area.

Bulk ore analyses from lithocap samples yielded low concentrations of Au and Ag, but significant enrichment in chalcophile elements such as Mo, Se, Bi, and Pb, which were probably introduced after the early event of acid leaching. Similar element anomalies are also reported from the advanced argillic alteration lithocap of Agia Barbara, in the broader Kassiteres–Sapes district, by Voudouris [23].

The fact that advanced argillic zones in the Konos Hill area display a more-or-less E–W trend, which follows the major tectonic orientation of the granodiorite emplacement, suggests that the SO_2- and HCl-bearing magmatic vapor may have ascended through these fault planes.

Close to the paleosurface, it condensed into surficial water and formed the advanced argillic alteration assemblages in a typical HS environment, in accordance with the findings of Holley et al. [68], who studied the Veladero Au–Ag HS epithermal mineralization. Moreover, the presence of the Konos Hill lithocap suggests that detailed mapping and mineralogical studies in hypogene advanced argillic alteration zones are critical, due to their common cogenetic and close spatial relations with porphyry-style mineralization in many prospects in Greece [23,29]. The presence of F-bearing phases such as zunyite, alunite, APS minerals, diaspore, and pyrophyllite at Konos Hill provides a potential vector towards possible hidden intrusions that may host porphyry-style mineralization.

5. Conclusions

The Konos Hill prospect represents a porphyry system genetically related to an intensively altered granodiorite intrusion and is overprinted by deep-level high-sulfidation mineralization. Alteration styles recognized include deep sericite and sodic–sericite assemblages associated with a quartz stockwork, which is overprinted by hypogene advanced argillic alteration. Quartz–alunite–APS–diaspore–kaolinite ± pyrophyllite and quartz–alunite–APS–zunyite–kaolinite ± pyrophyllite assemblages predominate. Transitional zones are typified by the presence of sericite. Electron microprobe data reveal wide variations in the composition of the alunite supergroup minerals. Alunite and natroalunite are widespread and are associated with APS minerals, which comprise members of the beudantite and plumbogummite subgroups and usually form in the cores of Na-rich alunite crystals. Common compositions include woodhouseite and svanbergite, whereas crandallite

and florencite are quite rare. Mineralization in the lithocap is characterized by a relative enrichment in chalcophile elements such as Bi, Mo, and Se, supporting the hypothesis of a spatial and temporal connection between the lithocap and the underlying porphyry-style mineralization. The presence of zunyite indicates that a F- and Cl-vapor ascended from the intrusive body under decreasing temperature conditions. Based on paragenetic relations and available literature data, a temperature of formation between 280–350 °C is likely for the studied assemblages. Zunyite (or other F-bearing phases, such as topaz) along with the presence of diaspore, pyrophyllite, and Sr- and REE-bearing APS minerals, could be used as an exploration tool, since they mark the proximity of the hypogene advanced argillic alteration zones to the porphyry environment.

Author Contributions: C.M. collected the studied samples. C.M. assisted by S.K. and J.B. acquired the mineral-chemical data and evaluated them along with P.V., P.G.S., V.M., T.B., R.M., T.B., T.M., and F.Z. C.M. wrote the manuscript. This paper is an extended version of a manuscript entitled "First zunyite-bearing lithocap in Greece: The case of the Konos Hill Mo–Cu–Re–Au porphyry system", that was published in the 1st Electronic Conference on Mineral Science, Sciforum, 2018. It is also part of the first author's Ph.D. thesis.

Funding: This research was partially funded by Eldorado Gold Corporation, 1188 Bentall 5 Burrard St., Vancouver, BC V6C 2B5, Canada.

Acknowledgments: The authors thank B. Schmitte for help provided during the microanalyses at the Institute of Mineralogy, University of Münster, and E. Galanopoulos for his assistance in drawing the maps. The editor and three anonymous reviewers who provided valuable comments that improved the manuscript are kindly thanked.

Conflicts of Interest: The authors declare no conflict of interest.

References

1. Halley, S.; Dilles, J.H.; Tosdal, R. *Footprints: The Hydrothermal Alteration and Geochemical Dispersion around Porphyry Copper Deposits*; SEG News Letter No. 100; Society of Economic Geologists (SEG): Littleton, CO, USA, 2015.
2. Heinrich, C. The physical and chemical evolution of low-salinity magmatic fluids at the porphyry to epithermal transition: A thermodynamic study. *Miner. Depos.* **2005**, *39*, 864–889, doi:10.1007/s00126-004-0461-9.
3. Gustafson, L.B.; Hunt, J.P. The porphyry copper deposit at El Salvador, Chile. *Econ. Geol.* **1975**, *70*, 857–912.
4. Sillitoe, R.H. Gold deposits in Western Pacific island arc: The magmatic connection. In *The Geology of Gold Deposits: The Perspective in 1988*; Keays, R., Ramsay, R., Groves, D., Eds.; Economic Geology Monograph Series; GeoScienceWorld: McLean, VA, USA, 1989; Volume 6, pp. 251–298.
5. Hedenquist, J.W.; Arribas, A.; Reynolds, T.J. Evolution of an intrusion-centered hydrothermal system: Far Southeast-Lepanto porphyry and epithermal Cu–Au deposis, Philippines. *Econ. Geol.* **1998**, *93*, 373–404.
6. Muntean, J.L.; Einaudi, M.T. Porphyry-epithermal transition: Maricunga Belt, Northern Chile. *Econ. Geol.* **2001**, *96*, 743–772.
7. Hedenquist, J.W.; Lowenstern, J.B. The role of magmas in the formation of hydrothermal ore deposits. *Nature* **1994**, *370*, 519–527.
8. Hedenquist, J.W.; Taran, Y.A. Modeling the formation of advanced argillic lithocaps: Volcanic vapor condensation above porphyry intrusions. *Econ. Geol.* **2013**, *108*, 1523–1540.
9. Sillitoe, R.H. Styles of high-sulphidation gold, silver and copper mineralization in the porphyry and epithermal environments. In *Proceedings of the PACRIM'99 Congress, Bali, Indonesia, 10–13 October 1999*; Weber, G., Ed.; Australasian Institute of Mining and Metallurgy: Parkville, VIC, Australia, 1999; pp. 29–44.
10. Watanabe, Y.; Aoki, M.; Yamamoto, K. Geology, age and style of the advanced argillic alteration in the Kobui area, Southwesterm Hokkaido, Japan. *Res. Geol.* **1997**, *47*, 263–281.
11. Meyer, C.; Hemley, J.J. Wall rock alteration. In *Geochemistry of Hydrothermal Ore Deposits*; Barnes, H.L., Ed.; Rinehart and Winston Holt: New York, NY, USA, 1967; pp. 166–235.
12. Stoffregen, R.E.; Alpers, C.N. Woodhouseite and svanbergite in hydrothermal ore deposits: Products of apatite destruction during advanced argillic alteration. *Can. Mineral.* **1987**, *25*, 201–211.

13. Seedorff, E.; Dilles, J.H.; Proffett, J.M.; Einaudi, M.T.; Zurcher, L.; Stavast, W.J.A.; Johnson, D.A.; Barton, M.D. Porphyry deposits: Characteristics and origin of hypogene features. In *100th Year Anniversary Issue*; Hedenquist, J.W., Thompson, J.F.G., Goldfarb, R.J., Richards, J.P., Eds.; Economic Geology; GeoScienceWorld: McLean, VA, USA, 2005, Volume 100, pp. 251–298.
14. Sillitoe, R.H. Porpyry copper systems. *Econ. Geol*. **2010**, *105*, 3–41, doi:10.2113 /gsecongeo.105.1.3.
15. Khashgerel, B.; Kavalieris, I.; Ken-Ichiro, H. Mineralogy, textures and whole-rock geochemistry of advanced argillic alteration: Hugo Dumett porphyry Cu–Au deposit, Oyu Tolgoi mineal district, Mongolia. *Econ. Geol.* **2008**, *71*, 849–863, doi:10.2113/gsecongeo.71.5.849.
16. Heinrich, C.A.; Driesner, T.; Stefansson, A.; Seward, T.M. Magmatic vapor contraction and the transport of gold from porphyry to epithermal ore deposits. *Geology* **2004**, *32*, 761–764, doi:10.1130/G20629.1
17. Shinohara, H.; Hedenquist, J. Constraints on magma degassing beneath the Far Southeast porphyry Cu–Au deposit, Philippines. *J. Petrol.* **1997**, *38*, 1741–1752.
18. Sillitoe, R. Erosion and collapse of volcanoes: Causes of telescoping in intrusion-centered ore deposits. *Geology* **1994**, *22*, 945–948, doi:10.1130/0091-7613(1994)022<0945:EACOVC>2.3.CO;2.
19. Milu, V.; Milesi, J.-P.; Leroy, J.L. Rosia Poieni copper deposit, Apuseni Mountains, Romania-advanced argillic overprint of a porphyry system. *Miner. Depos.* **2004**, *39*, 173–188.
20. Voudouris, P.; Spry, P.G.; Melfos, V.; Alfieris, D.; Mavrogonatos, C.; Repstock, A.; Djiba, A.; Stergiou, C.; Periferakis, A.; Melfou, M. Porphyry and Epithermal Deposits in Greece: A Review and New Discoveries. In Proceedings of the 8th Geochemistry Symposium, Antalya, Turkey, 2–6 May 2018.
21. Melfos, V.; Voudouris, P. Cenozoic metallogeny of Greece and potential for precious, critical and rare metals exploration. *Ore Geol. Rev*. **2017**, *59*, 1030–1057.
22. Voudouris, P.; Tarkian, M.; Arikas, K. Mineralogy of telluride-bearing epithermal ores in Kassiteres-Sappes area, western Thrace, Greece. *Mineral. Petrol*. **2006**, *87*, 31–52.
23. Voudouris, P. Hydrothermal corundum, topaz, diaspore and alunite supergroup minerals in the advanced argillic alteration lithocap of the Kassiteres-Sapes porphyry-epithermal system, western Thrace, Greece. *Neues Jahrbuch für Mineralogie* **2014**, *191*, 117–136.
24. Bissig, T.; Monecke, T.; Holley, E.A.; Leroux, G.; Voudouris, P.; Miškovic, A. Geochemical and quartz mineralogical vectors to epithermal ore in lithocaps in the TV Tower district, Biga peninsula, Turkey and Kassiteres-Sapes district, Greece. In Proceedings of the SEG-MJD Conference, Cesme, Turkey, 25–28 September 2016.
25. Kilias, S.P.; Naden, J.; Paktsevanoglou, M.; Giampouras, M.; Stavropoulou, A.; Apeiranthiti, D.; Mitsis, I.; Koutles, T.; Michael, K.; Christidis, C. Multistage alteration, mineralization and ore–forming fluid properties at the Viper (Sappes) Au–Cu–Ag–Te ore body, W. Thrace, Greece. *Bull. Geol. Soc. Greece* **2013**, *47*, 1635–1644, doi:10.12681/bgsg.11007.
26. Ortelli, M.; Moritz, R.; Voudouris, P.; Spangenberg, J. Tertiary porphyry and epithermal association of the Sapes-Kassiteres district, Eastern Rhodopes, Greece. In Proceedings of the 10th Biennial SGA Meeting, Townsville, Australia, 17–20 August 2009; pp. 536–538.
27. Voudouris, P.; Melfos, V.; Spry, P.G.; Bindi, L.; Moritz, R.; Ortelli, M.; Kartal, T. Extremely Re-rich molybdenite from porphyry Cu-Mo-Au prospects in northeastern Greece: Mode of occurrence, causes of enrichment, and implications for gold exploration. *Minerals* **2013**, *3*, 165–191.
28. Voudouris, P. Conditions of formation of the Mavrokoryfi high-sulfidation epithermal Cu–Ag–Au–Te deposit (Petrota Graben, NE Greece). *Miner. Petrol*. **2011**, *101*, 97–113.
29. Voudouris, P.; Melfos, V. Aluminum-phosphate-sulfate (APS) minerals in the sericitic-advanced argillic alteration zone of the Melitena porphyry-epithermal Mo–Cu ± Au ± Re prospect, western Thrace, Greece. *Neues Jahrbuch für Mineralogie* **2013**, *190*, 11–27.
30. Voudouris, P.; Alfieris, D. New porphyry-Cu ± Mo occurrences in northeastern Aegean/Greece: Ore mineralogy and transition to epithermal environment. In *Mineral Deposit Research: Meeting the Global Challenge*; Mao, J., Bierlein, F.P., Eds.; Springer: Berlin, Germany, 2005; pp. 473–476.
31. Fornadel, A.P.; Voudouris, P.; Spry, P.G.; Melfos, V. Mineralogical, stable isotope and fluid inclusion studies of spatially related porphyry Cu–Mo and epithermal Au–Te mineralization, Fakos Peninsula, Limnos Island, Greece. *Miner. Petrol.* **2012**, *105*, 85–111.

32. Periferakis, A.; Voudouris, P.; Melfos, V.; Mavrogonatos, C.; Alfieris, D. The Stypsi-Megala Therma porphyry-epithermal mineralization, Lesvos Island, Greece: New mineralogical and geochemical data. In *Geophysical Research Abstracts, Proceedings of the EGU General Assembly, Vienna, Austria, 23–28 April 2017*; EGU2017-12950; EGU: Vienna, Austria, 2017; Volume 19.
33. Kloprogge, J.T.; Frost, R.L. Raman and infrared microscopy study of zunyite, a natural Al13 silicate. *Spectrochim. Acta Part A Mol. Biomol. Spectrosc.* **1999**, *55*, 1505–1513.
34. Papoulis, D.; Tsolis-Katagas, P.; Katagas, C. New find of zunyite in advanced argillic alteration of rhyolites, Kos Island, South Aegean volcanic arc, Greece. *Bull. Geol. Soc. Greece* **2004**, *36*, 474–480.
35. Mavrogonatos, C.; Voudouris, P.; Spry, P.G.; Melfos, V.; Klemme, S.; Berndt, J.; Moritz, R.; Kanellopoulos, C. First zunyite-bearing lithocap in Greece: The case of Konos Hill Mo–Re–Cu–Au porphyry system. In *Proceedings of the 1st International Electronic Conference on Mineral Science, Sciforum, 16–31 July 2018*; MDPI AG: Basel, Switzerland, 2018; Volume 1, doi:10.3390/IECMS2018-05450.
36. Kydonakis, K.; Brunn, J.-P.; Sokoutis, D. North Aegean core complexes, the gravity spreading of a thrust wedge. *J. Geophys. Res. Solid Earth* **2015**, *120*, 595–616, doi:10.1002/2014JB011601.
37. Kydonakis, K.; Moulas, E.; Chatzitheodoridis, E.; Brunn, J.-P.; Kostopoulos, D. First-report on Mesozoic eclogite-facies metamorphism preceding Barrovian overprint from the western Rhodope (Chalkidiki, northern Greece). *Lithos* **2015**, *220–223*, 147–163, doi:10.1016/j.lithos.2015.02.007.
38. Ricou, L.E.; Burg, J.P.; Godfriaux, I.; Ivanov, Z. Rhodope and Vardari the metamorphic and the olistostromic paired belts related to the Cretaceous subduction under Europe. *Geodin. Acta* **1998**, *11*, 285–309.
39. Brun, J.P.; Faccenna, C. Exhumation of high-pressure rocks driven by slab rollback. *Earth Plan. Sci. Lett.* **2008**, *272*, 1–7, doi:10.1016/j.epsl.2008.02.038.
40. Wuthrich, E. Low Temperature Thermochronology of the North Aegean Rhodope Massif. Ph.D. Thesis, Swiss Federal Institute of Technology, Zurich, Switzerland, 2009.
41. Ring, U.; Glodny, J.; Will, T.; Thomson, S. The Hellenic subduction system: High pressure metamorphism, exhumation, normal faulting, and large-scale extension. *Annu. Rev. Earth Planet. Sci*. **2010**, *38*, 45–76.
42. Bonev, N.; Marchev, P.; Moritz, R.; Collings, D. Jurassic subduction zone tectonics of the Rhodope Massif in the Thrace region (NE Greece) as revealed by new U–Pb and $^{40}Ar/^{39}Ar$ geochronology of the Evros ophiolite and high-grade basement rocks. *Gondwana Res*. **2015**, *27*, 760–775.
43. Marchev, P.; Kaiser-Rohrmeier, B.; Heinrich, C.; Ovtcharova, M.; von Quadt, A.; Raicheva, R. Hydrothermal ore deposits related to post-orogenic extensional magmatism and core complex formation: The Rhodope Massif of Bulgaria and Greece. *Ore Geol. Rev*. **2005**, *27*, 53–89.
44. Jolivet, L.; Brunn, J.P. Cenozoic geodynamic evolution of the Aegean Region. *Int. J. Earth. Sci*. **2010**, *99*, 109–138.
45. Kilias, A.; Falalakis, G.; Sfeikos, A.; Papadimitriou, E.; Vamvaka, A.; Gkarlaouni, C. The Thrace basin in the Rhodope province of NE Greece—A Tertiary supra-detachment basin and its geodynamic implications. *Tectonophysics* **2013**, *595–596*, 90–105.
46. Ersoy, E.Y.; Palmer, M.R. Eocene-Quaternary magmatic activity in the Aegean: Implications for mantle metasomatism and magma genesis in an evolving orogeny. *Lithos* **2013**, *180–181*, 5–24.
47. Pe-Piper, G.; Piper, D.J.W. *The Igneous Rocks of Greece. The Anatomy of an Orogen*; Beiträge der Regionalen Geologie der Erde: Berlin, Germany, 2002; p. 573.
48. Moritz, R.; Márton, I.; Ortelli, M.; Marchev, P.; Voudouris, P.; Bonev, N.; Spikings, R.; Cosca, M. A review of age constraints of epithermal precious and base metal deposits of the Tertiary Eastern Rhodopes: Coincidence with Late Eocene-Early Oligocene tectonic plate reorganization along the Tethys. In *Proceedings of the XIX Congress Carpathian-Balkan Geological Association, Thessaloniki, Greece, 23–26 September 2010*; Christofides, G., Kantiranis, N.; Kostopoulos, D.S.; Chatzipetros, A. Eds.; Scientific Annals of the School of Geology, Aristotle University of Thessaloniki; Aristotle University of Thessaloniki: Thessaloniki, Greece, 2010; Volume 100, pp. 351–358.
49. Del Moro, A.; Innocenti, F.; Kyriakopoulos, C.; Manetti, P.; Papadopoulos, P. Tertiary granitoids from Thrace (Northern Greece): Sr isotopic and petrochemical data. *Neues Jahrbuch für Mineralogie* **1988**, *159*, 113–135.
50. Ortelli, M.; Moritz, R.; Voudouris, P.; Cosca, M.; Spangenberg, J. Tertiary porphyry and epithermal association of the Sapes-Kassiteres district, Eastern Rhodopes, Greece. In Proceedings of the 8th Swiss Geiscience Meeting, Fribourg, Switzerland, 19–20 November 2010.
51. Perkins, R.; Copper, F.J.; Condon, D.J.; Tattitsch, B.; Naden, J. Post-collisional Cenozoic extension in the northern Aegean: The high-K to shoshonitic intrusive rocks of the Maronia Magmatic Corridor, northeastern Greece. *Lithosphere* **2018**, 10, 582–601, doi:10.1130/L730.1.

52. Michael, C. *Geology and Geochemistry of Epithermal Gold Deposit in Konos Area*; Internal Report; IGME Xanthi: Madrid, Spain, 1993; Volume 75, p. 77.
53. Voudouris, P. Mineralogical, Geochemical and Fluid Inclusion Studies on Epithermal Vein Type Gold/Silver Mineralizations at Kassiteres/Sapes, (NE-Greece). Ph.D. Thesis, University of Hamburg, Hamburg, Germany, 1993.
54. Mavrogonatos, C.; Voudouris, P.; Spry, P.G.; Melfos, V.; Klemme, S.; Berndt, J.; Periferakis, A. Biotite Chemistry from Porphyry-Style Mineralization in Western Thrace, Greece. In Proceedings of the 8th Geochemistry Symposium, Antalya, Turkey, 2–6 May 2018.
55. Bridges, P.S.; Gordon, M.J.; Michael, C.; Ampatzioglou, M. Gold mineralization at Sappes, northern Greece. In *Europe's Major Gold Deposits*; Harvey, S., Ed.; Irish Association for Economic Geology: Dublin, Ireland, 1997; pp. 95–107.
56. Shawh, A.J.; Constantinides, D.C. The Sappes gold project. *Bull. Geol. Soc. Greece* **2001**, *34*, 1073–1080.
57. Michael, C. Epithermal systems and gold mineralization in Western Thrace, (North Greece). *Bull. Geol. Soc. Greece* **2004**, *36*, 416–423.
58. Jambor, J.L. Nomenclature of the alunite supergroup. *Can. Mineral.* **1999**, *37*, 1323–1341.
59. Dill, H.G. The geology of aluminium phosphates and sulfates of the alunite group minerals: A review. *Earth Sci. Rev.* **2001**, *53*, 35–93.
60. Mills, S.J.; Harter, F.; Nickel, E.H.; Ferraris, G. The standardization of mineral group hierarchies: Application to recent nomenclature proposals. *Eur. J. Mineral.* **2009**, *21*, 1073–1080.
61. Bayliss, P.; Kolitsch, U.; Nickel, E.H.; Pring, A. Alunite supergroup: Recommended nomenclature. *Mineral. Mag.* **2010**, *74*, 919–927.
62. Scott, K.M. Solid solution in, and classification of, gossan-derived members of the alunite-jarosite family, northwest Queensland, Australia. *Am. Mineral.* **1987**, *72*, 178–187.
63. Monecke, T.; Monecke, J.; Reynolds, T.J.; Tsuruoka, S.; Bennett, M.M.; Skewes, W.B.; Palin, R.M. Quartz Solubility in the H_2O-NaCl System: A Framework for Understanding Vein Formation in Porphyry Copper Deposits. *Econ. Geol.* **2018**, *113*, 1007–1046, doi:10.5382/econgeo.2018.4580.
64. Hikov, A.; Lerouge, C.; Velinova, N. Geochemistry of alunite group minerals in advanced argillic altered rocks from the Asarel porphyry copper deposit, Central Srednogorie. *Rev. Bulg. Geol. Soc.* **2010**, *71*, 133–148.
65. Reyes, A.G. Petrology of Philippine geothermal systems and the application of alteration mineralogy to their assessment. *J. Volcanol. Geotherm. Res.* **1990**, *43*, 279–309.
66. Reyes, A.G. *Mineralogy, Distribution and Origin of Aid Alteration in Philippine Geothermal Systems*; Geological Survey of Japan Report; Geological Survey of Japan: Tsukuba, Japan, 1991.
67. Chang, Z.; Hedenquist, J.W.; White, N.C.; Cooke, D.R.; Roach, M.; Deyell, C.; Garcia, J., Jr.; Gemmell, J.B.; Mcknight, S.; Cuisone, A.L. Exploration tools for linked porphyry and epithermal deposits: Example from the Mankayan intrusion-centered Cu-Au District, Luzon, Philippines. *Econ. Geol.* **2011**, *106*, 1365–1398.
68. Holley, E.A.; Monecke, T.; Bissig, T.; Reynolds, T.J. Evolution of High-Level Magmatic-Hydrothermal Systems: New Insights from Ore Paragenesis of the Veladero High-Sulfidation Epithermal Au-Ag Deposit, El Indio-Pascua Belt, Argentina. *Econ. Geol.* **2017**, *112*, 1747–1771, doi:10.5382/econgeo.2017.4528.